



OPEN

# Dynamic behaviors of approximately ellipsoidal microbubbles photothermally generated by a graphene oxide-microheater

SUBJECT AREAS:

FLUID DYNAMICS

OPTICAL MANIPULATION AND  
TWEEZERSReceived  
16 April 2014Accepted  
29 July 2014Published  
15 August 2014

Correspondence and requests for materials should be addressed to X.X. (xingxiaobo@scnu.edu.cn) or D.Z. (zhudb@scnu.edu.cn)

\* These authors contributed equally to this work.

Xiaobo Xing<sup>1\*</sup>, Jiapeng Zheng<sup>2\*</sup>, Fengjia Li<sup>1</sup>, Chao Sun<sup>1</sup>, Xiang Cai<sup>3</sup>, Debin Zhu<sup>1</sup>, Liang Lei<sup>4</sup>, Ting Wu<sup>3</sup>, Bin Zhou<sup>2</sup>, Julian Evans<sup>2</sup> & Ziyi Chen<sup>2</sup>

<sup>1</sup>Education Ministry's Key Laboratory of Laser Life Science & Institute of Laser Life Science, College of Biophotonics, South China Normal University, Guangzhou, Guangdong, 510631, China, <sup>2</sup>Centre for Optical and Electromagnetic Research, South China Academy of Advanced Optoelectronics, South China Normal University, 510006 Guangzhou, China, <sup>3</sup>Department of Light chemical engineering, Guangdong Polytechnic, Foshan, 528041, China, <sup>4</sup>School of Physics and Optoelectronic Engineering, Guangdong University of Technology, Guangzhou 510006, China.

**Thermal microbubbles generally grow directly from the heater and are spherical to minimize surface tension. We demonstrate a novel type of microbubble indirectly generated from a graphene oxide-microheater. Graphene oxide's photothermal properties allowed for efficient generation of a thermal gradient field on the microscale. A series of approximately ellipsoidal microbubbles were generated on the smooth microwire based on heterogeneous nucleation. Other dynamic behaviors induced by the microheater such as constant growth, directional transport and coalescence were also investigated experimentally and theoretically. The results are not only helpful for understanding the bubble dynamics but also useful for developing novel photothermal bubble-based devices.**

Microscale bubbles have found many applications in medical imaging<sup>1</sup>, biomedical analysis<sup>2</sup>, drug delivery<sup>3</sup>, and microfluidic elements<sup>4–7</sup>. Various methods have been adopted to generate microbubbles, including ultrasonic cavitation<sup>8</sup>, laser induced cavitation<sup>9,10</sup>, microfluidic flow-focusing<sup>11</sup>, and liquid boiling<sup>12</sup>. Photothermal heaters produced by laser light combined together with photothermal materials can carry on localized heating to initiate the phase transition of the liquid<sup>13–18</sup>. Previous reports have shown that the microbubbles can be successfully produced by using highly focused laser beams or optical fiber to illuminate photothermal substrates<sup>13–15</sup>, liquids<sup>16</sup>, and nanoparticles<sup>17,18</sup>. Compared with other systems<sup>8–11</sup>, photothermal system allows for accurately controlling the forming location and the status of microbubbles. The microheater has a dominant influence on the growth and movement of microbubbles. For example, it has demonstrated that the growth rate of microbubbles can be tuned by the power of the microheater<sup>15,16</sup>. The microbubbles are attracted towards the microheater by thermocapillary forces and Marangoni forces<sup>14,19</sup>. So far, the reported photothermal microbubbles were generated directly on the microheater<sup>13–18</sup>. Whether the microbubbles can be emerged away from the microheater? It is an interesting topic, which has not been detailedly explored.

Our previous study has been demonstrated a novel microscale photothermal heater based on the combination of a microwire and graphene oxide (GO)<sup>20</sup>. GO nanosheets (GONs) in N,N-Dimethylformamide (DMF) solvent were successfully trapped and deposited on the surface of the microwire with enhanced evanescent fields<sup>21–24</sup> by injecting near-infrared light into the microwire. The GO-deposition exhibited strong photothermal properties<sup>25–29</sup>, serving as a line-shaped heater with a length of several hundred micrometers. When the superheat limit of liquid was reached, a lot of spherical microbubbles with diameters from tens to hundreds of micrometers were generated directly on the GO-microheater immersed in DMF, which is a common phenomenon in a traditional photothermal system<sup>13–18</sup>. The present work is devoted to novel microbubbles with approximately ellipsoidal shapes that produced on the smooth microwire rather than on the microheater. Similar to liquid drops on thin wires<sup>30,31</sup>, each microbubble exhibited a symmetrical conformation with respect to the microwire axis. Bubble behaviors induced by the microheater including constant growth, directional transport, and coalescence were investigated experimentally and theoretically, showing the similar behaviors to the reported photothermal



microbubble<sup>14,19</sup>. The existence of the approximately ellipsoidal microbubbles will gain new insight into the mechanism of bubble formation and bubble dynamics at the microscale.

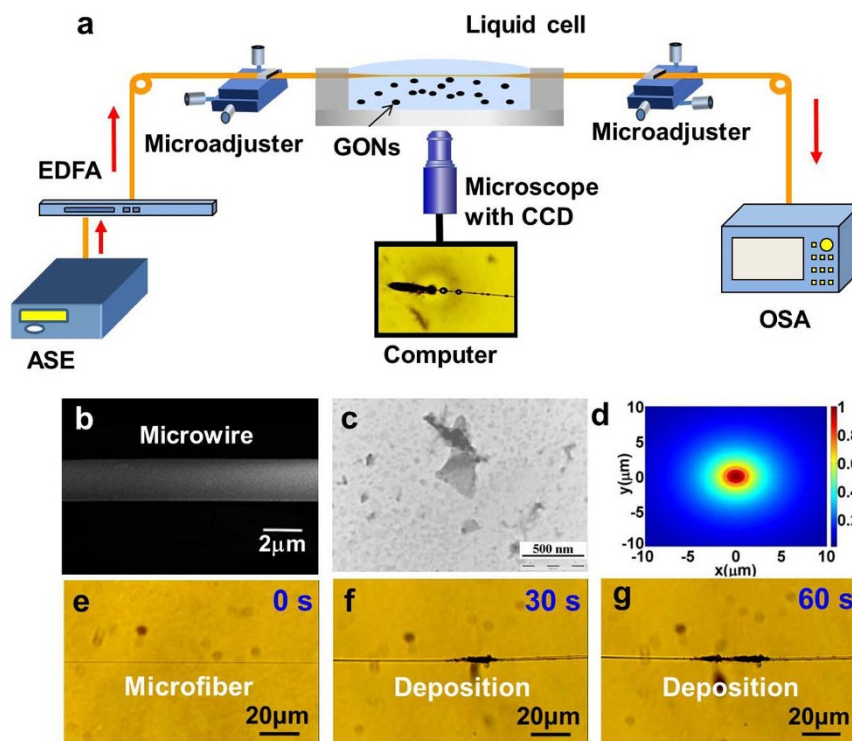
## Results

Figure 1a shows schematic illustration of experimental setup to obtain GO-microheater. An inverted optical microscope with a charge-coupled device (CCD) camera was used for real-time monitoring. A liquid cell was mounted on an x-y manual translation stage of the microscope. A 2.2- $\mu\text{m}$  diameter, 2.0-mm long microwire was fabricated by drawing a single mode optical fiber (SMF-28, Corning Inc.) using two stepper motors through the flame-heated technique. The microwire was immersed in the GONs-DMF suspension and fixed by two microadjusters. Figure 1b shows a scanning electron microscopy (SEM) image of 2.2- $\mu\text{m}$ -diameter wire with good surface smoothness. An amplified spontaneous emission broadband light source (ASE,  $\sim 20$  mW, 1527–1566 nm) was excited by an erbium-doped fiber amplifier (EDFA, 1546–1562 nm), whose output power was 40 mW at 1527–1566 nm. Light from EDFA was coupled into the microwire, and output spectra were recorded by an optical spectrum analyzer (OSA, Yokogawa AQ 6370C) with a resolution of 0.02 nm. Transmission electron microscopy (TEM, Fig. 1c) and SEM (see supplementary information, Fig. S1) images show that GONs have scale-like shape with micrometer long wrinkles. In the experiment, the concentration of GONs-DMF suspension was optimized at 0.05 mg/ml. Since a higher concentration could affect imaging due to absorption, and a lower concentration would limit the quantity of GO-deposition.

Mode characteristics of the microwire were analyzed in the supplementary information, demonstrating a 2.2- $\mu\text{m}$ -diameter wire submerged in DMF produced a tight field confinement and strong evanescent field. Figure 1d shows a 2D field profile of the  $\text{HE}_{11}$  mode at wavelength of 1550 nm. Effective diameter of mode field ( $D_{\text{eff}}$ ) and power ratio outside the microwire ( $\eta$ ) of a 2.2- $\mu\text{m}$ -diameter wire

were 12.23–13.76  $\mu\text{m}$  and 86.59–88.32% at wavelength of 1527–1566 nm (see supplementary information, Fig. S1). When the light propagated along the microwire, the evanescent field outside the microwire was absorbed by GONs, producing a thermal gradient based on effective optical-to-thermal energy conversion of GONs<sup>20</sup>. And then a weak convective flow was generated, driving the randomly dispersed GONs to swim into the evanescent field near the microwire<sup>32,33</sup>. Subsequently, the GONs near the microwire were trapped and deposited on the microwire by an optical gradient force. The process of the deposition would go on until the laser was turned off. Figures 1e–h show optical microscope images of the deposition with light launched for 0, 30 s, and 60 s. Finally, a GO-microheater with length of 282  $\mu\text{m}$  and maximum width of 75  $\mu\text{m}$  was formed within 3.5 min. Note that it is not necessary to form the GO-microheater in certain location of the microwire. The location of the microheater in the liquid can be adjusted by tuning microwire through two microadjusters.

In the experiment, the DMF liquid surface was convex due to surface tension<sup>34</sup>. When the microwire was immersed into the liquid, it could be divided into three sections (AE, ED and DF as indicated in Fig. 2a) under capillarity effect<sup>34</sup>. The two microwire segments AE and DF were located at DMF-air interface while the microwire segment ED including GO-microheater BC was immersed in the GONs-DMF suspension. Based on our previous study, the working GO-microheater was capable of initiating the phase transition of its surrounding DMF. As a result, spherical microbubbles were generated directly on the GO-microheater (see supplementary information, Fig. S2). By tuning microwire through two microadjusters, the microwire segment A'C including the GO-microheater BC and microwire segment D'F' were located at the DMF-air interface and microwire segment CD' was immersed in the GONs-DMF suspension (as shown in Fig. 2b). In this case, it was difficult to generate microbubbles on the GO-microheater, which was suspended at the DMF-air interface. Instead, a series of microbubbles were produced



**Figure 1** | (a) Schematic of experimental setup. An inverted optical microscope with a CCD camera was used for real-time monitoring. The ASE source excites the EDFA, and then light from EDFA is coupled into the microwire. (b) SEM image of 2.2  $\mu\text{m}$ -diameter microwire shows good surface smoothness. (c) TEM image of GONs shows a scale-like structure. (d) A 2D field profile of 2.2  $\mu\text{m}$ -diameter microwire under fundamental modes ( $\text{HE}_{11}$ ) at the wavelength of 1550 nm. (e–f) Optical microscope images of the GO-deposition with light launched for 0, 30 s, and 60 s, respectively.

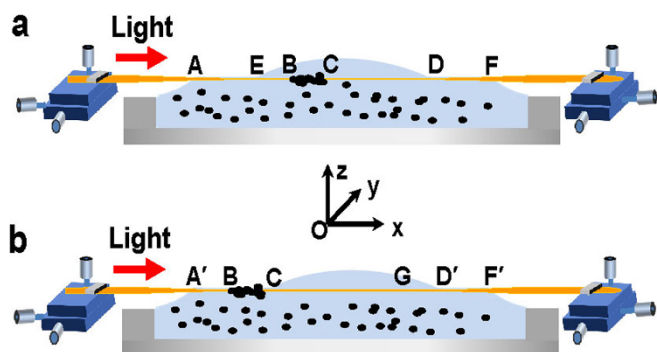


**Figure 2** | (a) Before adjusting, the two microwire segments AE and DF were located at the DMF-air interface and the microwire segment ED including GO-microheater BC was immersed in the GONs-DMF suspension. (b) After adjusting microwire, the microwire segment A'C including the GO-microheater BC and the microwire segment D'F' were located at the DMF-air interface, and microwire segment CD' was immersed in the GONs-DMF suspension. Red arrows show the direction of light propagation.

along a horizontal microwire axis on right side of the GO-microheater. As shown in Fig. 3, each microbubbles exhibited a symmetrical conformation with respect to the microwire axis and took a shape of approximate ellipsoid. Similar to liquid drops on thin wires<sup>30,31</sup>, the microbubble conformation could be characterized by two parameters: long axis ( $L$ ) and short axis ( $S$ ), which were measured horizontally and vertically with respect to the microwire.

Growth, directional transport, disappearance, emergence, and coalescence were the types of dynamic microbubble behaviors, visually observed along the microwire. Figure 3 illustrates a growth period of microbubble  $A_0$  closest to the GO-microheater at a magnification of  $100\times$  (with frames taken from movie S1). Microbubble  $A_0$  emerged at  $t = 08'09''$  in Fig. 3a, and kept growing

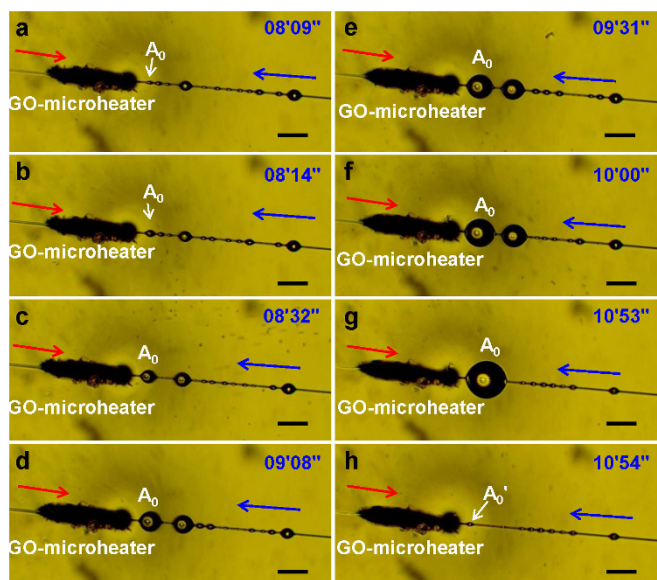


**Figure 3** | Optical microscopy images for the growth process of microbubble  $A_0$  at a magnification of  $100\times$  after the light was turned on (a) at  $t = 08'09''$ , (b)  $t = 08'14''$ , (c)  $t = 08'32''$ , (d)  $t = 09'08''$ , (e)  $t = 09'31''$ , (f)  $t = 10'00''$ , (g)  $t = 10'53''$ , (h)  $t = 10'54''$ , detailed process from  $t = 08'09''$  to  $10'54''$  was shown in movie (Movie S1, supplementary information). Red and blue arrows represent the directions of light propagation and microbubbles movement, respectively. The scale bar represents  $100\ \mu\text{m}$ .

until it reached a maximum size at  $t = 10'53''$  (Fig. 3g), and then exploded. Afterwards, a new small microbubble  $A_0'$  with size of  $L = 24\ \mu\text{m}$ ,  $S = 14\ \mu\text{m}$  was generated at  $t = 10'54''$  (Fig. 3h). Table 1 shows that the sizes ( $L$ ,  $S$ ) of microbubble  $A_0$  are ( $22\ \mu\text{m}$ ,  $14\ \mu\text{m}$ ), ( $38\ \mu\text{m}$ ,  $26\ \mu\text{m}$ ), ( $61\ \mu\text{m}$ ,  $47\ \mu\text{m}$ ), ( $81\ \mu\text{m}$ ,  $71\ \mu\text{m}$ ), ( $97\ \mu\text{m}$ ,  $83\ \mu\text{m}$ ), ( $109\ \mu\text{m}$ ,  $95\ \mu\text{m}$ ), and ( $143\ \mu\text{m}$ ,  $128\ \mu\text{m}$ ), respectively, at  $t = 08'09''$ ,  $08'14''$ ,  $08'32''$ ,  $09'08''$ ,  $09'31''$ ,  $10'00''$ , and  $10'53''$ . At the same time, other small microbubbles grew large and moved towards GO-microheater which was opposite the direction of the light propagation. Meanwhile, the GO-microheater expanded towards the left along the microwire. This is because the optical trapping occurred at the left side of GO-microheater where the microwire was not covered by GONs and remained a strong optical gradient force. Table 1 shows that the lengths of the GO-microheater are  $300$ ,  $312$ ,  $313$ ,  $319$ ,  $322$ ,  $339$ ,  $341$ , and  $351\ \mu\text{m}$ , respectively, at  $t = 08'09''$ ,  $08'14''$ ,  $08'32''$ ,  $09'08''$ ,  $09'31''$ ,  $10'00''$ ,  $10'53''$ , and  $10'54''$ , respectively, while the width did not noticeably change.

Other dynamic behaviors such as coalescence and transport were observed. As shown in Fig. 4 (which contains frames from movie S2 at magnification of  $250\times$ ), microbubble  $A_1$  gradually grew up, staying motionless. Figure 4a–4d illustrate the orderly movement of the microbubbles  $B_2$ ,  $B_3$ , and  $B_4$ . It can be seen that there was a vacancy between microbubble  $B_1$  and  $B_2$  at  $t = 04'24''$  (Fig. 4a). At  $t = 04'25''$ , microbubble  $B_2$  moved to the left by  $23\ \mu\text{m}$ , occupied the vacancy and left another vacancy (Fig. 4b). Following, microbubbles  $B_3$  and  $B_4$  in turn moved to the left by  $20\ \mu\text{m}$  and  $22\ \mu\text{m}$  at  $t = 04'26''$  and  $t = 04'27''$ , respectively (Fig. 4c and 4d). Figure 4e and 4f describe collective disappearance and emergence of the microbubbles. At  $t = 04'28''$ , microbubbles  $B_2$ ,  $B_3$  and  $B_4$  disappeared (Fig. 4e). At  $t = 04'29''$ , new microbubbles  $B_6$ ,  $B_7$ ,  $B_8$ , and  $B_9$  emerged at the right side of microbubble  $B_1$  (Fig. 4f). Figure 4g–4l show coalescence of the microbubbles. At  $t = 04'39''$ , five microbubbles  $C_1$ ,  $C_2$ ,  $C_3$ ,  $C_4$ , and  $C_5$  were closely arranged along the microwire (Fig. 4g). At  $t = 04'40''$ , the  $C_5$  with size of ( $19\ \mu\text{m}$ ,  $14\ \mu\text{m}$ ) moved towards  $C_4$  ( $16\ \mu\text{m}$ ,  $10\ \mu\text{m}$ ), and coalesced into a larger microbubble  $C_6$  ( $21\ \mu\text{m}$ ,  $16\ \mu\text{m}$ ) in Fig. 4h. And then, all microbubbles stayed at their positions at  $t = 04'41''$  and  $t = 04'42''$  (Fig. 4i and 4j). After that, microbubble  $C_3$  ( $24\ \mu\text{m}$ ,  $16\ \mu\text{m}$ ) moved towards  $C_2$  ( $24\ \mu\text{m}$ ,  $18\ \mu\text{m}$ ), and then coalesced into a larger microbubble  $C_7$  ( $31\ \mu\text{m}$ ,  $21\ \mu\text{m}$ ) at  $t = 04'43''$ , meanwhile, microbubble  $C_6$  moved left by  $23\ \mu\text{m}$  (Fig. 4k). Following, microbubble  $C_7$  moved towards  $C_1$  ( $28\ \mu\text{m}$ ,  $17\ \mu\text{m}$ ), and then coalesced into a larger microbubble  $C_8$  ( $36\ \mu\text{m}$ ,  $26\ \mu\text{m}$ ), while microbubble  $C_6$  remained motionless (Fig. 4l). This shows that coalescence of microbubbles is one of the reasons for the growth of the microbubbles.

## Discussion

As described in section 3, the GO-deposition as a line-shaped microheater was located at the DMF-air interface. After a period of light illumination within  $60\ \text{s}$ , the temperature on the GO-microheater was estimated to be  $425.95\ \text{K}$ , the boiling point of the DMF. When the GO-microheater operated, the temperature distribution in the surrounding DMF was governed by the thermal transfer equation

**Table 1** | The sizes ( $L$ ,  $S$ ) of microbubble  $A_0$  and the lengths of the GO-microheater at  $t = 08'09''$ ,  $08'14''$ ,  $08'32''$ ,  $09'08''$ ,  $09'31''$ ,  $10'00''$ , and  $10'53''$ , respectively

Time	Sizes of microbubble $A_0$	Lengths of GO-microheater
$08'09''$	( $22\ \mu\text{m}$ , $14\ \mu\text{m}$ )	$300\ \mu\text{m}$
$08'14''$	( $38\ \mu\text{m}$ , $26\ \mu\text{m}$ )	$312\ \mu\text{m}$
$08'32''$	( $61\ \mu\text{m}$ , $47\ \mu\text{m}$ )	$313\ \mu\text{m}$
$09'08''$	( $81\ \mu\text{m}$ , $71\ \mu\text{m}$ )	$319\ \mu\text{m}$
$09'31''$	( $97\ \mu\text{m}$ , $83\ \mu\text{m}$ )	$322\ \mu\text{m}$
$10'00''$	( $109\ \mu\text{m}$ , $95\ \mu\text{m}$ )	$339\ \mu\text{m}$
$10'53''$	( $143\ \mu\text{m}$ , $128\ \mu\text{m}$ )	$341\ \mu\text{m}$

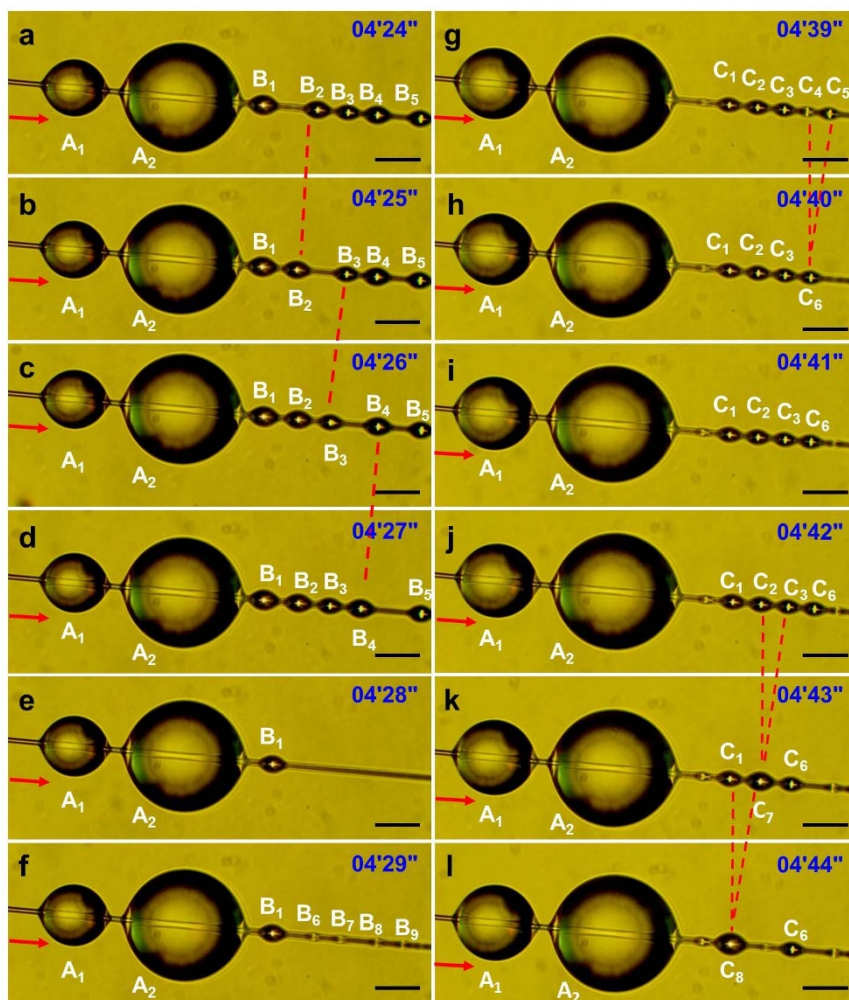


**Figure 4** | Optical microscope images of dynamic processes of microbubbles at a magnification of 250 $\times$ , detailed process from  $t = 02'29''$  to  $t = 04'46''$  is shown in movie (Movie S2, supplementary information). (a)–(d) Microbubbles  $B_2$ ,  $B_3$ , and  $B_4$  orderly moved to the left from  $t = 04'24''$  to  $04'27''$ . (e) Microbubbles  $B_2$ ,  $B_3$ ,  $B_4$  and  $B_5$  disappeared at  $t = 04'28''$ . (f) New microbubbles  $B_6$ ,  $B_7$ ,  $B_8$  and  $B_9$  were generated at  $t = 04'29''$ . (g) At  $t = 04'39''$ , the microbubbles were at their original positions. (h) At  $t = 04'40''$ ,  $C_4$  and  $C_5$  mixed together to form  $C_6$ . (i), (j) At  $t = 04'41''$  and  $04'42''$ , all microbubbles remained the same with those of at  $t = 04'40''$ . (k) At  $t = 04'43''$ ,  $C_2$  and  $C_3$  mixed together to form  $C_7$ . (l) At  $t = 04'44''$ ,  $C_1$  and  $C_7$  mixed together to form  $C_8$ . The scale bar represents 50  $\mu\text{m}$ .

$$\nabla \cdot (-k\nabla T + \rho C_p T \vec{u}) = Q \quad (1)$$

where  $k$  is thermal conductivity ( $\text{W}/(\text{m}\cdot\text{K})$ ),  $T$  is temperature (K),  $\nabla T$  is temperature gradient (K),  $C_p$  is heat capacity ( $\text{J}/(\text{kg}\cdot\text{K})$ ), and  $Q$  ( $\text{W}/\text{m}^3$ ) represents a source term such as GO-microheater<sup>35</sup>. The temperature field in the GONs-DMF suspension was simulated using finite-element modeling software in COMSOL Multiphysics 4.3 (supplementary information, Fig. S3). Figure 5a shows the partial temperature distribution around the GO-microheater in a rectangular area (in Fig. S3b) circled by lines  $y = \pm 300 \mu\text{m}$ ,  $x = 0$ , and  $x = 1000 \mu\text{m}$ . The temperature was from 364.53 K to 425.95 K. Figure 5b shows the vertical temperature distribution for  $x = 400, 450, 500, 600,$  and  $800 \mu\text{m}$ . It can be seen that the vertical temperature distribution is symmetric with respect to the axis of the microwire ( $y = 0$ ). Figure 5c shows the horizontal temperature distribution for  $y = 0, \pm 10, \pm 30, \pm 50, \pm 70,$  and  $\pm 100 \mu\text{m}$ . It is clear that temperature decreases with the distance from the GO-microheater. The absolute value of slope decreases with the distance from the GO-microheater in Fig. 5c, producing a decreased temperature gradient along the microwire axis from the left to the right.

The approximately ellipsoidal microbubbles were generated on the microwire away from the microheater. Here the physical mech-

anism of the microbubble generation can be explained by heterogeneous nucleation. As one of the most important processes in bubble nucleation, heterogeneous nucleation normally occurs at phase boundaries. At these sites, the effective surface energy is lower, which diminishes the free energy barrier and finally facilitates nucleation<sup>36,37</sup>. There were DMF vapors in the liquid under the GO-microheater. The microwire surface was the phase boundary in this system, so it could provide preferential sites to facilitate nucleation. Meanwhile, the solubility of the DMF vapors decreased with the increasing temperature in the suspension. The DMF vapors were persistently separated and finally integrated into the nucleus at the microwire segment CG in Fig. 2b. The overall result is that the heterogeneous nucleation and vapor integration act cooperatively to facilitate the generation and growth of microbubbles. In addition, we observed that there were other sites on the microwires segment GD' (in Fig. 2b) which can facilitate heterogeneous nucleation. However, these nuclei failed to grow up because they were farther away from the GO-microheater (supplementary information, Fig. S4). Therefore, the microbubble growth is linked closely with the temperature. Microbubbles would sometimes translate along the wire once growth stopped. After the microbubble vanished from its location induced by explosion,

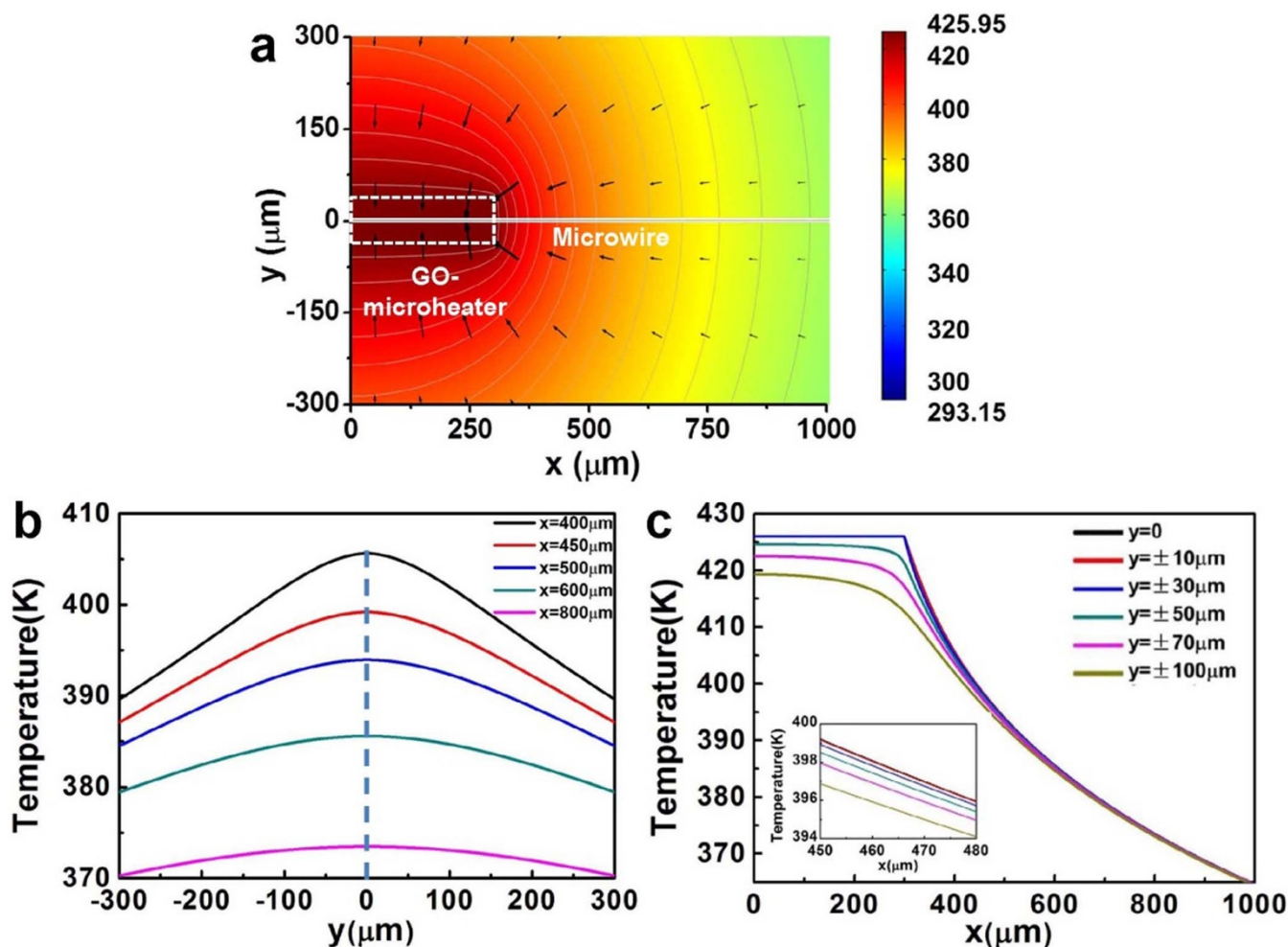


**Figure 5** | (a) Simulation of temperature distribution driven by the GO-microheater. Black arrows show the direction of temperature gradient. The isotherms are indicated by gray lines. (b) The vertical temperature distribution on lines  $x = 400, 450, 500, 600,$  and  $800 \mu\text{m}$ . (c) The horizontal temperature distribution on lines  $y = 0, \pm 10, \pm 30, \pm 50, \pm 70,$  and  $\pm 100 \mu\text{m}$ . The inset of Fig. 5b shows the amplified temperature distribution from  $x = 450$  to  $480 \mu\text{m}$ .

movement, or coalescence, a new one was formed and circulated the process mentioned above.

The movement of the microbubbles was dominated by driving forces and resistance forces, as shown in Fig. 6. One of possible

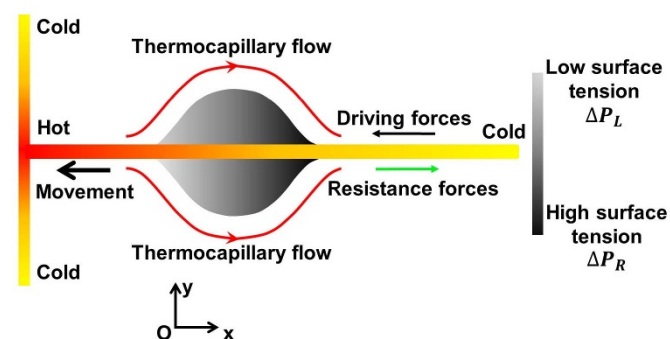


**Figure 6** | Mechanism of a microbubble movement on the microwire. There are driving forces (indicated by the black arrow) and resistance forces (indicated by the green arrow) on the microbubble. The driving force comes from the temperature gradient along the interface of microbubble, which can be thought of as a thermocapillary force arising from thermocapillary flow indicated by red arrows, and a non-equilibrium Laplace pressure difference.

driving mechanisms comes from thermocapillary effect<sup>38,39</sup>. As described in Fig. 5a, there is a temperature gradient along the interface of the microbubble. In DMF liquid, surface tension decreases linearly with the increasing temperature<sup>40,41</sup>. So it is accompanied by a corresponding surface tension gradient at the microbubble interface, which induces the resulting interfacial shear stress  $\tau_S$ . The interfacial shear stress is proportional to the temperature gradient  $\nabla T_S$  and described by  $\tau_S = -\sigma_T \cdot \nabla T_S$ , where  $\sigma_T$  is the temperature coefficient of surface tension<sup>42,43</sup>. As illustrated in Fig. 6, the difference in interfacial shear stress drives thermocapillary flow along the microbubble interface (indicated by red arrow), which is oriented from low to high surface tension and opposite to the temperature gradient. The reverse force of the momentum transfer induced by the thermocapillary flow causes the microbubble to move toward high temperature regions, such as the GO-microheater. The thermocapillary force can be expressed by the surface integral of shear stress on the microbubble interface<sup>38,39</sup>:

$$F_C = -\iint \sigma_T \frac{dT}{dr} dS \quad (2)$$

where  $\frac{dT}{dr}$  is the temperature gradient along the microbubble interface,  $dS$  is the surface element on the microbubble interface.

Another possible driving mechanism arises from the non-equilibrium Laplace pressure difference<sup>44</sup>. According to the Young-

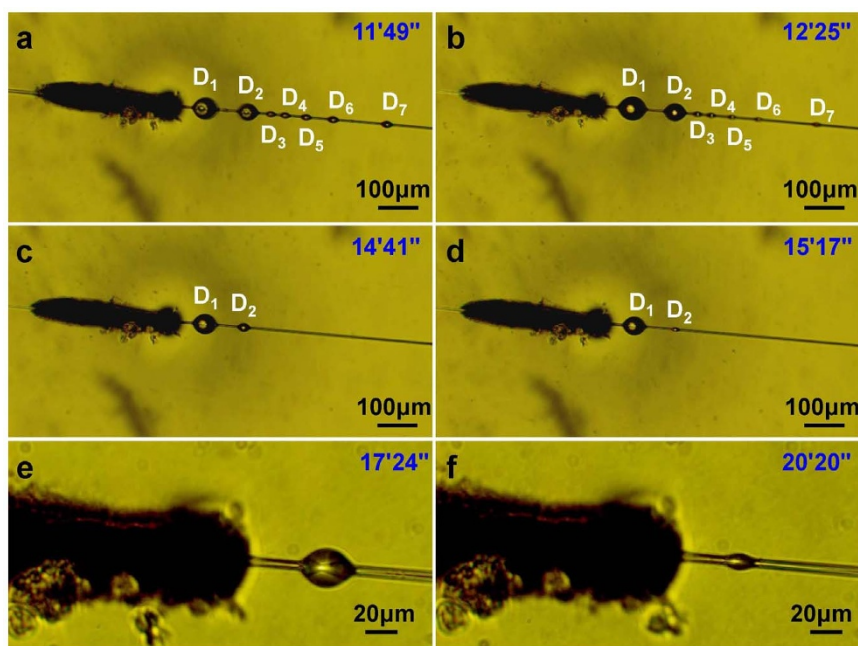


**Figure 7** | Optical microscope images for disappearance process of microbubbles at magnifications of 100× (a–d) and 400× (e, f), respectively, when the light was turned off at  $t = 11'49''$  (a),  $12'25''$  (b),  $14'41''$  (c),  $15'17''$  (d),  $17'24''$  (e), and  $20'20''$  (f).

Laplace equation, the Laplace pressure difference on the two sides of the microbubble along microwire can be expressed analytically as<sup>34</sup>

$$\Delta P_L = \sigma(T_L) \cdot \left( \frac{1}{R_1} + \frac{1}{R_2} \right) \quad (3)$$

$$\Delta P_R = \sigma(T_R) \cdot \left( \frac{1}{R_1} + \frac{1}{R_2} \right) \quad (4)$$

where  $\Delta P_L$  and  $\Delta P_R$  are the Laplace pressure differences, and  $\sigma(T_L)$  and  $\sigma(T_R)$  are the surface tensions on the left and right side of the microbubble, respectively.  $R_1$  and  $R_2$  are the radii of the curvature of the surface. As presented in Fig. 6, the Laplace pressure difference on the right side ( $\Delta P_R$ ) is larger than that on the left side ( $\Delta P_L$ ) because the surface tension on the right side  $\sigma(T_R)$  is larger than that on the left side  $\sigma(T_L)$ . The resultant non-equilibrium Laplace pressure difference can propel the microbubble to move toward the region with lower Laplace pressure difference<sup>44</sup>.

Meanwhile, there are several resistance forces such as viscous force from DMF liquid and friction force from microwire. Consequently, various motion states were as a result of the interaction of these forces. Several microbubbles remained stationary on the microwire when the driving forces couldn't overcome the resistance forces (such as microbubble  $A_1$ ,  $A_2$ ,  $B_1$ , and  $B_5$  shown in Fig. 4a–f). Others kept on moving towards the microheater when the driving forces dominated over the resisting forces (such as microbubbles  $B_2$ ,  $B_3$ , and  $B_4$  in Fig. 4a–d). Two adjacent microbubbles could have differing translation rates, causing a collision with each other and finally coalescence into a bigger bubble. As an example, microbubble  $C_2$  and  $C_3$  mixed together to form  $C_7$  in Fig. 4k–l. According to the statistics from movie S2, there are altogether 66 microbubbles generated from  $t = 02'29''$  to  $t = 04'46''$ , among which, 46 ones coalesced or transported to the microheater, 2 ones transported away from the microheater, and 18 ones remain stationary. Figure S5 (supplementary information) shows the details on transport and coalescence of microbubbles generated on another microwire with diameter of 7.0  $\mu\text{m}$ , demonstrating that the phenomena can be repeatable.

Our observations show that the temperature distribution induced by GO-microheater plays a significant role in the dynamic behaviors of approximately ellipsoidal microbubbles. After the light source was

cut off, the temperature on the microheater was gradually decreasing due to Newtonian heat flow and no more source term. Consequently, it was unable to provide adequate heat to maintain the dynamic behaviors of microbubbles, and then microbubbles started to gradually disappear and/or shrink. The temperature was initially lower at further distances from the GO-microheater, which resulted in the faster disappearance of microbubbles. As shown in Fig. 7a–7f, at first, five microbubbles  $D_3$ ,  $D_4$ ,  $D_5$ ,  $D_6$ , and  $D_7$  started to shrink gradually until they disappeared, while  $D_1$  and  $D_2$  remained unchanged with sizes ( $L$ ,  $S$ ) of (72  $\mu\text{m}$ , 47  $\mu\text{m}$ ) and (55  $\mu\text{m}$ , 45  $\mu\text{m}$ ), respectively, as shown in Fig. 7a and 7b. The sizes of microbubbles varied from  $D_3$  (24  $\mu\text{m}$ , 14  $\mu\text{m}$ ),  $D_4$  (26  $\mu\text{m}$ , 15  $\mu\text{m}$ ),  $D_5$  (26  $\mu\text{m}$ , 18  $\mu\text{m}$ ),  $D_6$  (29  $\mu\text{m}$ , 18  $\mu\text{m}$ ),  $D_7$  (31  $\mu\text{m}$ , 19  $\mu\text{m}$ ) to  $D_3$  (23  $\mu\text{m}$ , 14  $\mu\text{m}$ ),  $D_4$  (25  $\mu\text{m}$ , 13  $\mu\text{m}$ ),  $D_5$  (19  $\mu\text{m}$ , 12  $\mu\text{m}$ ),  $D_6$  (17  $\mu\text{m}$ , 10  $\mu\text{m}$ ),  $D_7$  (20  $\mu\text{m}$ , 10  $\mu\text{m}$ ), respectively. And then, the left two microbubbles  $D_1$  and  $D_2$  started to shrink after the other microbubbles disappeared.  $D_2$  had the quicker velocity of disappearance due to the faster decreasing temperature of  $D_2$ . The sizes of  $D_1$  were (63  $\mu\text{m}$ , 51  $\mu\text{m}$ ) in Fig. 7c, (58  $\mu\text{m}$ , 47  $\mu\text{m}$ ) in Fig. 7d, (41  $\mu\text{m}$ , 33  $\mu\text{m}$ ) in Fig. 7e, (23  $\mu\text{m}$ , 15  $\mu\text{m}$ ) in Fig. 7f, respectively. In the experiment, we found that  $D_2$  disappeared at  $t = 16'31''$ . The sizes of  $D_2$  in Fig. 7c and 7d were (41  $\mu\text{m}$ , 33  $\mu\text{m}$ ) and (23  $\mu\text{m}$ , 15  $\mu\text{m}$ ), respectively.

In conclusion, we have presented that various dynamic behaviors of microbubbles with novel conformation under the GO-microheater system. The surrounding liquid was heated to form a temperature gradient field by GO-microheater based on the photothermal effects. A series of approximately ellipsoidal microbubbles were formed and grew symmetrically along the microwire axis on the right side of the GO-microheater based on heterogeneous nucleation. Meanwhile, several microbubbles were found to continuously move towards the GO-microheater or coalesce together under the temperature gradient field. We contributed the driving force of directional transport to thermocapillary effect or non-equilibrium Laplace pressure along the microbubble. When the light was turned off, microbubbles stopped moving and started to shrink gradually. The results revealed that GO-microheater played a significant role in the dynamic behaviors of approximately ellipsoidal microbubbles. It has been demonstrated a new experimental case on microbubble generation with other conformations, which would be not only helpful for under-



standing the bubble dynamics but also for development of novel photothermal bubble-based devices. However, the detailed mechanism on the symmetrical conformation of the microbubble is requiring further exploration.

## Methods

**Fabrication of optical microwire.** A microwire was fabricated by drawing a single mode optical fiber (SMF-28, Corning Inc.) using two stepper motors through the flame-heated technique<sup>45</sup>.

**Preparation and characteristics of GO.** Graphite powders (spectral pure) were purchased from Sinopharm Chemical Reagent Co., Ltd. The reagents and solvents were obtained from commercial suppliers. All aqueous solutions were prepared with ultrapure water (>18 M $\Omega$ ) from a Milli-Q Plus system (Millipore). GO was prepared by oxidizing natural graphite powder based on a modified Hummers method<sup>46,47</sup>. As-prepared GO was dialyzed to remove the residual salts and acids completely, and the resulting purified GO powder was collected by centrifugation and then dried in the air. GO powder was suspended in ultrapure water (0.5 mg/ml) and exfoliated through ultrasonication in a water bath (KQ218, 60 W) for 3 hours. As a result, the bulk of GO powder was transformed into GONs.

GONs were characterized using SEM, Fourier transform infrared (FTIR) spectra and UV/vis absorption spectra (see supplementary information, Fig. S6–S9). Transmission electron microscopy (TEM, Fig. 1c) and SEM (see supplementary information, Fig. S6) images show that GONs have scale-like shape with micrometer long wrinkles. The dried GO was transformed into GONs through ultrasonication for 3 hours in a water bath, and well dispersed in DMF due to the presence of oxygen-containing groups in GONs<sup>48,49</sup>. The near-infrared (NIR) absorption spectra are sensitive to the concentration of GONs in the DMF solvent (see supplementary information, Fig. S6). Inset of Fig. S9 shows relationship between the absorbance and the concentration of GONs dispersion at the wavelength of 1550 nm. It can be seen that the absorption grows linearly with the concentration.

- Lindner, J. R. Microbubbles in medical imaging: current applications and future directions. *Nat. Rev. Drug Discov.* **3**, 527–532 (2004).
- Prentice, P., Cuschierp, A., Dholakia, K., Prausnitz, M. & Campbell, P. Membrane disruption by optically controlled microbubble cavitation. *Nat. Phys.* **1**, 107–110 (2005).
- Tsutsui, J. M., Xie, F. & Porter, R. T. The use of microbubbles to target drug delivery. *Cardiovasc. Ultrasound* **2**, 23–23 (2004).
- Ting-Hsiang, W., Lanyu, G., Yue, C., Wei, K. & Pei-Yu, C. Pulsed laser triggered high speed microfluidic switch. *Appl. Phys. Lett.* **93**, 144102 (2008).
- Prakash, M. & Gershenfeld, N. Microfluidic bubble logic. *Science* **315**, 832–835 (2007).
- Ahmed, D., Mao, X., Juluri, B. K. & Huang, T. J. A fast microfluidic mixer based on acoustically driven sidewall-trapped microbubbles. *Microfluid. Nanofluid.* **7**, 727–731 (2009).
- Marmottant, P. & Hilgenfeldt, S. A bubble-driven microfluidic transport element for bioengineering. *Proc. Natl. Acad. Sci. U. S. A.* **101**, 9523–9527 (2004).
- Hong, C., Wayne, K., Andrew, A. B., Michael, R. B. & Thomas, J. M. Blood vessel deformations on microsecond time scales by ultrasonic cavitation. *Phys. Rev. Lett.* **106**, 034301 (2011).
- Detlef, L. Cavitation physics: Lasers blow a bigger bubble. *Nature* **392**, 21 (1998).
- Quinto-Su, P. A., Huang, X. H., Gonzalez-Avila, S. R., Wu, T. & Ohl, C. D. Manipulation and microrheology of carbon nanotubes with laser-induced cavitation bubbles. *Phys. Rev. Lett.* **104**, 014501 (2010).
- Hettiarachchi, K., Talu, E., Longo, M. L., Dayton, P. A. & Lee, A. P. On-chip generation of microbubbles as a practical technology for manufacturing contrast agents for ultrasonic imaging. *Lab Chip* **7**, 463–468 (2007).
- Tsai, J. H. & Lin, L. W. Transient thermal bubble formation on polysilicon micro-resistors. *J. Heat Transfer* **124**(2), 375–382 (2002).
- Ohta, A. T., Jamshidi, A., Valley, J. K., Hsu, H.-Y. & Wu, M. C. Optically actuated thermocapillary movement of gas bubbles on an absorbing substrate. *Appl. Phys. Lett.* **91**, 074103 (2007).
- Zheng, Y. *et al.* Accumulating microparticles and direct-writing micropatterns using a continuous-wave laser-induced vapor bubble. *Lab Chip* **11**, 3816–3820 (2011).
- Zhang, K. *et al.* Laser-induced thermal bubbles for microfluidic applications. *Lab Chip* **11**, 1389–1395 (2011).
- Xu, R. *et al.* Photothermal formation and targeted positioning of bubbles by a fiber taper. *Appl. Phys. Lett.* **101**, 054103 (2012).
- Liu, Z., Hung, W. H., Aykol, M., Valley, D. & Cronin, S. B. Optical manipulation of plasmonic nanoparticles, bubble formation and patterning of SERS aggregates. *Nanotechnology* **21**, 105304 (2010).
- Lapotko, D. Optical excitation and detection of vapor bubbles around plasmonic nanoparticles. *Opt. Express* **17**, 2538–2556 (2009).
- Hu, W., Ishii, K. S. & Ohta, A. T. Micro-assembly using optically controlled bubble microrobots. *Appl. Phys. Lett.* **99**, 094103 (2011).
- Xing, X. *et al.* Graphene oxide-deposited microfiber: a new photothermal device for various microbubble generation. *Opt. Express* **21**, 31862–31871 (2013).
- Brambilla, G. *et al.* Optical manipulation of microspheres along a subwavelength optical wire. *Opt. Letters* **32**, 3041–3043 (2007).
- Yang, A. H. J. *et al.* Optical manipulation of nanoparticles and biomolecules in sub-wavelength slot waveguides. *Nature* **457**, 71–75 (2009).
- Skelton, S. E. *et al.* Evanescent wave optical trapping and transport of micro- and nanoparticles on tapered optical fibers. *J. Quant. Spectrosc. Radiat. Transf.* **113**, 2512–2520 (2012).
- Sheu, F.-W. & Yen-Si, H. Trapping and propelling microparticles at long range by using an entirely stripped and slightly tapered no-core optical fiber. *Sensors* **13**, 2884–2894 (2013).
- Yang, K. *et al.* Graphene in mice: ultrahigh in vivo tumor uptake and efficient photothermal therapy. *Nano Lett.* **10**, 3318–3323 (2010).
- Robinson, J. T. *et al.* Ultrasmall reduced graphene oxide with high near-infrared absorbance for photothermal therapy. *J. Am. Chem. Soc.* **133**, 6825–6831 (2011).
- Tian, B., Wang, C., Zhang, S., Feng, L. & Liu, Z. Photothermally enhanced photodynamic therapy delivered by nano-graphene oxide. *ACS Nano* **5**, 7000–7009 (2011).
- Zhang, W. *et al.* Synergistic effect of chemo-photothermal therapy using PEGylated graphene oxide. *Biomaterials* **32**, 8555–8561 (2011).
- Markovic, Z. M. *et al.* In vitro comparison of the photothermal anticancer activity of graphene nanoparticles and carbon nanotubes. *Biomaterials* **32**, 1121–1129 (2011).
- Carroll, B. J. Equilibrium conformations of liquid drops on thin cylinders under forces of capillarity. A theory for the roll-up process. *Langmuir* **2**, 248–250 (1986).
- Carroll, B. J. The accurate measurement of contact angle, phase contact areas, drop volume, and Laplace excess pressure in drop-on-fiber systems. *J. Colloid. Interf. Sci.* **57**, 488–495 (1976).
- Louchev, O. A., Juodkakis, S., Murazawa, N., Wada, S. & Misawa, H. Coupled laser molecular trapping, cluster assembly, and deposition fed by laser-induced Marangoni convection. *Opt. Express* **16**, 5673–5680 (2008).
- Wilson, B. K., Hegg, M., Miao, X., Cao, G. & Lin, L. Y. Scalable nano-particle assembly by efficient light-induced concentration and fusion. *Opt. Express* **16**, 17276–17281 (2008).
- De Gennes, P.-G., Brochard-Wyart, F. & Quéré, D. Capillarity and wetting phenomena: drops, bubbles, pearls, waves. *Springer* 2004.
- Miao, X., Wilson, B. K. & Lin, L. Y. Localized surface plasmon assisted microfluidic mixing. *Appl. Phys. Lett.* **92**, 124108 (2008).
- Liu, X. Heterogeneous nucleation or homogeneous nucleation? *J. Chem. Phys.* **112**, 9949–9955 (2000).
- Hienola, A., Vehkamäki, H., Riipinen, I. & Kulmala, M. Homogeneous vs. heterogeneous nucleation in water-dicarboxylic acid systems. *Atmos. Chem. Phys.* **9**, 1873–1881 (2009).
- Lu, J. & Peng, X. Bubble slippage on thin wires during subcooled boiling. *Int. J. Heat Mass Tran.* **49**, 2337–2346 (2006).
- Christopher, D. M. & Jiang, J. Bubble sweeping and interactions on wires during subcooled boiling. *Int. J. Heat Mass Tran.* **52**, 5020–5028 (2009).
- Abubaker, A. M., Khaled, H. A. E. A., Mohammad, S. A. & Adel, S. A. Viscosity and surface tension of binary systems of N,N-dimethylformamide with alkan-1-ols at different temperatures. *J. Chem. Thermodynamics* **56**, 106–113 (2013).
- Kahl, H., Wadewitz, T. & Winkelmann, J. Surface tension of pure liquids and binary liquid mixtures. *J. Chem. Eng. Data* **48**, 580–586 (2003).
- Vela, E., Hafez, M. & Régnier, S. Laser-induced thermocapillary convection for mesoscale manipulation. *Int. J. Optomechatron.* **3**, 289–302 (2009).
- Basu, A. S. & Gianchandani, Y. B. Shaping high-speed Marangoni flow in liquid films by microscale perturbations in surface temperature. *Appl. Phys. Lett.* **90**, 034102 (2007).
- Zheng, Y. *et al.* Directional water collection on wetted spider silk. *Nature* **463**, 640–643 (2010).
- Tong, L. *et al.* Subwavelength-diameter silica wires for low-loss optical wave guiding. *Nature* **426**, 816–819 (2003).
- Kovtyukhova, N. I. *et al.* Layer-by-layer assembly of ultrathin composite films from micron-sized graphite oxide sheets and polycations. *Chem. Mater.* **11**, 771–778 (1999).
- Hummers Jr, W. S. & Offeman, R. E. Preparation of graphitic oxide. *J. Am. Chem. Soc.* **80**, 1339–1339 (1958).
- Cai, X. *et al.* Sodium 1-naphthalenesulfonate-functionalized reduced graphene oxide stabilizes silver nanoparticles with lower cytotoxicity and long-term antibacterial activity. *Chem.-Asian J.* **7**, 1664–1670 (2012).
- Cai, X. *et al.* Synergistic antibacterial brilliant blue/reduced graphene oxide/quaternary phosphonium salt composite with excellent water solubility and specific targeting capability. *Langmuir* **27**, 7828–7835 (2011).

## Acknowledgments

The work thanks for Prof. Da Xing from Education Ministry's Key Laboratory of Laser Life Science & Institute of Laser Life Science, College of Biophotonics, South China Normal University, for his support in experiments. This work was supported by Natural Science Foundation of China (61177077, 61107029, 21006038, 81371877, 81071790, 61307053), Postdoctoral Science Foundation Funded Project of China (201003359), and Guangdong Excellent Doctoral Dissertation Funded Project (SYBZZM201126).



## Author contributions

X.X. designed the present study; J.Z. and F.L. constructed the experimental setup and performed the experiments; X.X. and C.S. performed its data analyses and wrote the manuscript; X.C., D.Z., L.L. and T.W. contributed to preparation and characterization of graphene oxide, B.Z., J.E. and Z.C. contributed to the revision of the manuscript. All authors reviewed the manuscript.

## Additional information

**Supplementary information** accompanies this paper at <http://www.nature.com/scientificreports>

**Competing financial interests:** The authors declare no competing financial interests.

**How to cite this article:** Xing, X. *et al.* Dynamic behaviors of approximately ellipsoidal microbubbles photothermally generated by a graphene oxide-microheater. *Sci. Rep.* **4**, 6086; DOI:10.1038/srep06086 (2014).



This work is licensed under a Creative Commons Attribution-NonCommercial-NoDerivs 4.0 International License. The images or other third party material in this article are included in the article's Creative Commons license, unless indicated otherwise in the credit line; if the material is not included under the Creative Commons license, users will need to obtain permission from the license holder in order to reproduce the material. To view a copy of this license, visit <http://creativecommons.org/licenses/by-nc-nd/4.0/>